

## PAPER

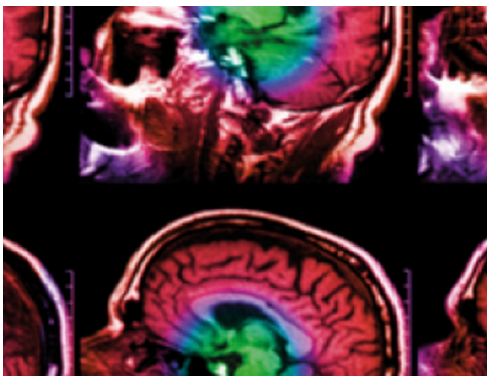
Fragmentation of 120 and 200 MeV  $u^{-1}$   $^4\text{He}$  ions  
in water and PMMA targetsTo cite this article: M Rovituso *et al* 2017 *Phys. Med. Biol.* **62** 1310View the [article online](#) for updates and enhancements.

## Related content

- [Secondary radiation measurements for particle therapy applications: nuclear fragmentation produced by  \$^4\text{He}\$  ion beams in a PMMA target](#)  
M Marafini, R Paramatti, D Pinci *et al.*
- [Investigation of mixed ion fields in the forward direction for 220.5 MeV/u helium ion beams: comparison between water and PMMA targets](#)  
G Aricò, T Gehrke, J Jakubek *et al.*
- [Nuclear physics in particle therapy: a review](#)  
Marco Durante and Harald Paganetti

## Recent citations

- [Are Further Cross Section Measurements Necessary for Space Radiation Protection or Ion Therapy Applications? Helium Projectiles](#)  
John W. Norbury *et al*
- [Challenges in Monte Carlo Simulations as Clinical and Research Tool in Particle Therapy: A Review](#)  
S. Muraro *et al*
- [Beam characterization at NSRL for radiobiological experiments—phase 1](#)  
L. Burigo *et al*

**IPEM | IOP**

Series in Physics and Engineering in Medicine and Biology

Your publishing choice in medical physics,  
biomedical engineering and related subjects.Start exploring the collection—download the  
first chapter of every title for free.

# Fragmentation of 120 and 200 MeV $u^{-1}$ $^4\text{He}$ ions in water and PMMA targets

M Rovituso<sup>1,7</sup>, C Schuy<sup>1</sup>, U Weber<sup>1</sup>, S Brons<sup>2</sup>,  
M A Cortés-Giraldo<sup>3</sup>, C La Tessa<sup>4,7</sup>, E Piasetzky<sup>5</sup>, D Izraeli<sup>5</sup>,  
D Schardt<sup>1</sup>, M Toppi<sup>6</sup>, E Scifoni<sup>1,7</sup>, M Krämer<sup>1</sup>  
and M Durante<sup>1,7</sup>

<sup>1</sup> GSI Helmholtzzentrum für Schwerionenforschung, Darmstadt, Germany

<sup>2</sup> Heidelberger Ionenstrahl-Therapiezentrum (HIT), Heidelberg, Germany

<sup>3</sup> University of Seville, Spain

<sup>4</sup> Nasa Space Radiation Laboratory, Brookhaven National Laboratory, Upton, NY, USA

<sup>5</sup> University of Tel Aviv, Israel

<sup>6</sup> Laboratori Nazionali di Frascati LNF—INFN, Frascati, Italy

<sup>7</sup> TIFPA Trento Institute for Fundamental Physics and Applications—INFN Trento, Italy

E-mail: [marco.durante@tifpa.infn.it](mailto:marco.durante@tifpa.infn.it)

Received 29 August 2016, revised 7 December 2016

Accepted for publication 9 December 2016

Published 23 January 2017



## Abstract

Recently, the use of  $^4\text{He}$  particles in cancer radiotherapy has been reconsidered as they potentially represent a good compromise between protons and  $^{12}\text{C}$  ions. The first step to achieve this goal is the development of a dedicated treatment planning system, for which basic physics information such as the characterization of the beam lateral scattering and fragmentation cross sections are required. In the present work, the attenuation of  $^4\text{He}$  primary particles and the build-up of secondary charged fragments at various depths in water and polymethyl methacrylate were investigated experimentally for 120 and 200 MeV  $u^{-1}$  beams delivered by the synchrotron at the Heidelberg Ion-Beam Therapy Center, Heidelberg. Species and isotope identification was accomplished combining energy loss and time-of-flight measurements. Differential yields and energy spectra of all fragments types were recorded between  $0^\circ$  and  $20^\circ$  with respect to the primary beam direction.

Keywords: particle therapy, helium ions, nuclear fragmentation

(Some figures may appear in colour only in the online journal)

## Introduction

External beam radiation therapy is one of the key features in modern multi-modal cancer cure (Durante and Loeffler 2010). Over 50% of all patients with localized malignant tumors undergo treatment with ionizing radiation, either alone or in combination with surgery and chemotherapy (Loeffler and Durante 2013). Following the increasing popularity of heavy ions in tumor therapy,  $^4\text{He}$  ions have regained the interest of the medical community as a compromise between protons and  $^{12}\text{C}$  ions (Tommasino *et al* 2015). Although 2054 patients have been treated with  $^4\text{He}$  beams at Lawrence Berkeley Laboratory (LBL) (Berkeley CA, US) between 1975 and 1992, a comprehensive database of basic physics measurements in the therapeutic energy range for treatment planning development and verification is still missing.

From a biological and physical point of view,  $^4\text{He}$  ions present a trend in between protons and  $^{12}\text{C}$  ions. The most important aspects of  $^4\text{He}$  from a radiotherapy perspective are: (i) a reduction of the relative biological effectiveness (RBE) in the Bragg peak region compared to  $^{12}\text{C}$  ions (Grün *et al* 2015); (ii) a reduction in energy straggling (Bragg peak width) as well as a reduction in multiple scattering (beam spot broadening reduced by factor of four, see figure 1) compared to protons (Weber and Kraft 2009).

Together with the processes mentioned above, primary ions might undergo nuclear break up when colliding with other nuclei along their path towards the tumor site. Nuclear fragmentation results in the production of a complex mixed field of fragments with lower charge and different energy than the primary radiation, which is translated in a dose tail extending beyond the Bragg peak, as shown in figure 2.  $^4\text{He}$  ions suffer less projectile fragmentation than  $^{12}\text{C}$  ions, and their tail is mainly composed of hydrogen (H) isotopes with similar penetration depth.

Treatment planning systems require a deep knowledge of all the aforementioned physical processes for accurately modeling the primary beam interactions in the patient's body (Durante and Paganetti 2016).

Due to its unique nuclear structure, fragmentation of  $^4\text{He}$  projectiles cannot be described with the abrasion-ablation model (Schardt *et al* 2010) used for all other heavy ions. This approach is replaced by a one-step process of direct reaction (Cucinotta *et al* 1993), where the total, absorption and elastic cross sections are estimated with an optical model approach, while fragmentation cross sections is predicted with a semi-empirical two-body dissociation model. The latter has been recently implemented in treatment planning for particles (TRiP98) (Krämer *et al* 2016) for its extension to  $^4\text{He}$  beams.

In this work, nuclear fragmentation of 120 and 200 MeV  $\text{u}^{-1}$   $^4\text{He}$  ions in thick water and PMMA targets has been experimentally investigated. The loss of primary ions (attenuation) and the fragments build-up at increasing target depths as well as the yields and kinetic energy spectra of all secondary fragments at several angles are presented. The aim of this study is to validate the new dedicated model for  $^4\text{He}$  ions in TRiP98 and to provide data for benchmarking Monte Carlo transport codes in the projectile-energy region where experimental data are missing (Burigo *et al* 2014, Taleei *et al* 2016).

A complementary work has been performed in collaboration by Mairani *et al*. They report on a study of double differential yields of secondary H fragments emerging from PMMA targets at three different  $^4\text{He}$  beam energies.

The results of both studies might be of interest in other aspects of ion therapy, e.g. for improving pencil beam algorithms as the one developed by Fuchs *et al* (2012) and for Monte Carlo treatment planning algorithms as the one described by Mairani *et al* (2016).

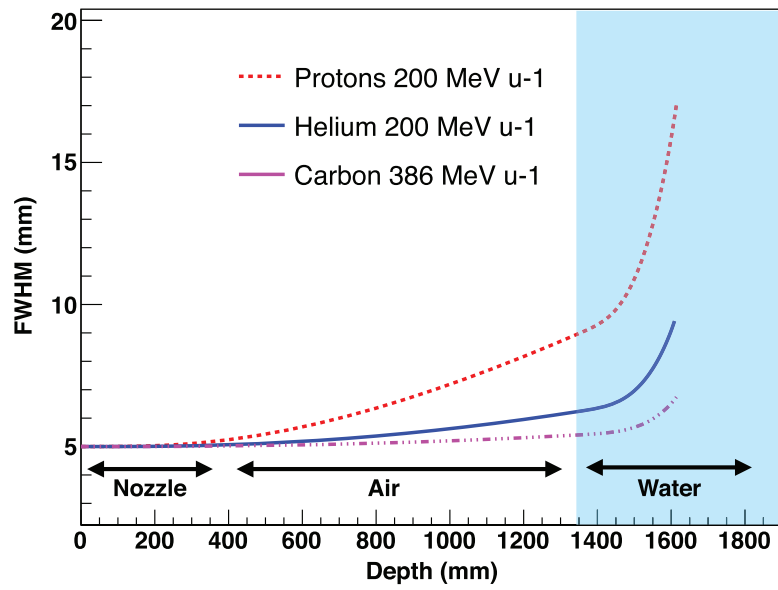


**Figure 1.** Calculated spread-out of pencil beams for p, <sup>4</sup>He, <sup>12</sup>C from a nozzle geometry comparable with the ion beam therapy setup at GSI (Schardt *et al* 2010) and with the recent ion-beam facilities, like University Clinics of Marburg and Heidelberg. A parallel beam entering the water absorber (the patient blue area) at 1 m of distance from the nozzle exit has been simulated.

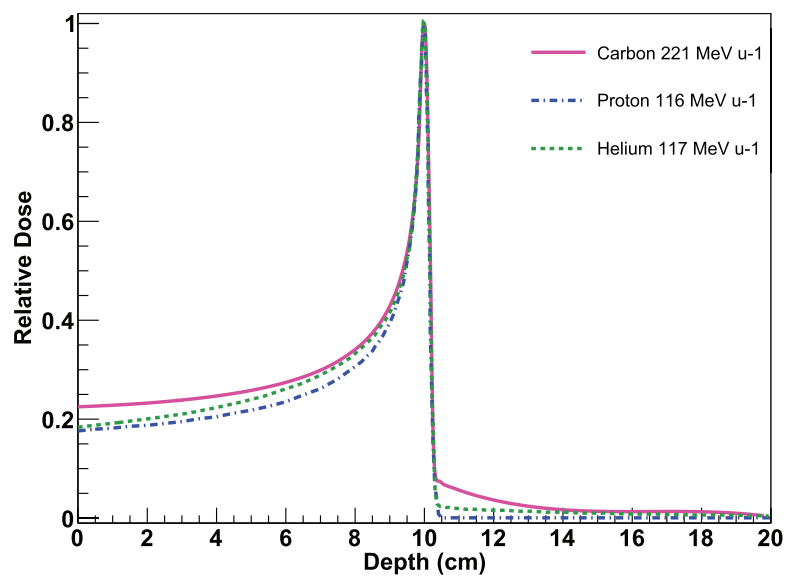


**Figure 2.** Depth dose profile of protons, <sup>4</sup>He and <sup>12</sup>C ions in water calculated with TRiP98.

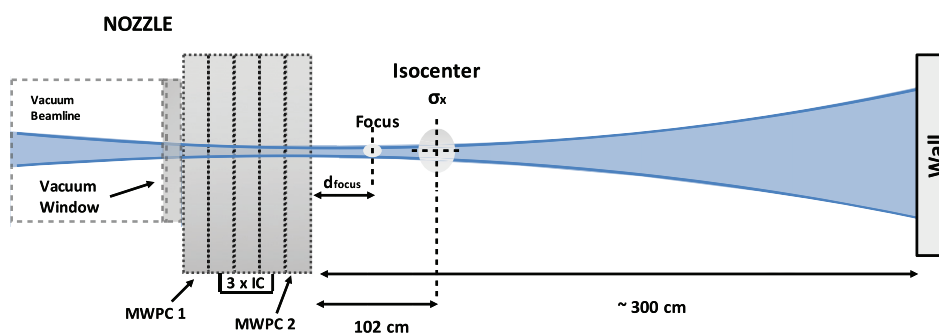


**Figure 3.** Scheme of the nozzle in QS cave HIT. The figure is not to scale. The vacuum exit window is composed of 2 Mylar foils for a thickness of  $100\ \mu\text{m}$  each and Kevlar tissue of  $0.012\ \text{g cm}^{-2}$ . The two multi-wire proportional chamber (MWPC) and the three ionization chamber (IC) have a thickness of 40 mm each. The pencil beam envelope is defined by the two filled lines in blue. The focus point given by the two quadrupole magnets placed at  $\sim 10\ \text{m}$  upstream was found to be approximately at 50 cm from the nozzle.

## 1. Experimental setup

Two main experiments were performed in this work: the attenuation of the primary beam together with the build-up of secondary fragments and the double differential yields (yield and kinetic energy spectrum at different angles) of the remaining  $^4\text{He}$  and secondary fragments.

### 1.1. Ion beam characteristics

All measurements were performed at the experimental beam line at HIT (Haberer *et al* 2004). The primary  $^4\text{He}$  beam was delivered through the therapeutic beam monitoring nozzle (figure 3) composed of a vacuum exit window and 5 monitoring chambers for a total of 1.80 mm water equivalent thickness.

Beam envelopes at energies of 120 and 200  $\text{MeV u}^{-1}$  have been measured with EDR2 x-rays films (Zhu *et al* 2002) and analyzed in order to get information on the beam focus, ion optics, scattering in air and beam divergency. The profile obtained at the isocenter results in a Gaussian distribution with a full width at half maximum (FWHM) of 9.5 and 5.6 cm and a beam divergence of 3.0 and 2.5 mrad for 120 and 200  $\text{MeV u}^{-1}$ , respectively.

### 1.2. Targets

When fragmentation cross sections are measured the ratio between amount of target material (in this case water) and amount of ‘container material’ has to be minimized. For this reason three different targets have been optimized and used for the experiments.

- (i) Two types of polystyrene flasks (large and medium) manufactured by COSTAR. The former size had outer dimensions  $11.90 \times 20.00 \times 4.22\ \text{cm}^3$  and wall thickness 0.42 cm while the latter size had outer dimensions  $8.33 \times 9.01 \times 3.48\ \text{cm}^3$  and wall thickness 0.32 cm. The water equivalent thickness (further referred to as  $\text{cm H}_2\text{O}$ ) of each flask was measured with the PTW peak finder (PTW 2015) and was found to be  $4.28 \pm 0.01\ \text{cm}$  for the large flask and  $3.49 \pm 0.01$  for the medium flask.

- (ii) A set of custom designed water targets (vessels produced by the Nasa Space Radiation Laboratory at Brookhaven National Laboratory, Upton, NY, US) of 1, 3 and 3.5 cm H<sub>2</sub>O with thin (less than 1 mm) vessel-wall material and a circular shape of 5.2 cm diameter.
- (iii) PMMA blocks of 20 × 20 cm<sup>2</sup> area and thickness 5 cm or 5.78 ± 0.01 cm H<sub>2</sub>O.

The thicknesses necessary for measuring the beam attenuation were obtained with a combination of the NSRL targets and large flasks (>4 cm H<sub>2</sub>O) for water and stacks of blocks for PMMA. The angular distribution measurements were acquired with 4.28 cm H<sub>2</sub>O and 13.92 cm H<sub>2</sub>O targets, equal to half of the maximum penetration depth of 120 and 200 MeV u<sup>-1</sup> <sup>4</sup>He beams, respectively.

### 1.3. Detectors arrangement

Three kind of detectors were selected for the experiments:

- (i) a 1 mm thick plastic scintillator (BC400 type) coupled with an Hamamatsu R6427 Photomultiplier (PMT) (further referred to as SC1);
- (ii) a 5 mm plastic scintillator (BC400 type) hexagonally shaped with a 5 cm inscribed radius and coupled with an Hamamatsu R6427 PMT (further referred to as ΔE);
- (iii) a 14 cm long BaF<sub>2</sub> crystal hexagonally shaped with a 4.37 cm inscribed radius, surrounded by 1 mm thick Aluminum case and coupled with Thorn EMI 9821 QB PMT (further referred to as E).

The detector arrangement for measuring the primary beam attenuation is shown in figure 4(a). The number of <sup>4</sup>He ions incident on the target was monitored by SC1 while the number of out-coming helium (He) and H fragments was identified by a combination of the ΔE and the E detectors signals (telescope system (Carboni *et al* 2012)). The target center was positioned at isocenter (see figure 3) and the telescope was aligned to the central beam axis. The telescope was placed as close as possible to the target to maximize its acceptance angle and thus minimize the loss of fragments due to lateral scattering.

The yield and energy spectra of secondary fragments emerging from the target were assessed by simultaneous measurements of energy loss in the telescope and the time-of-flight (TOF) technique (Weimar *et al* 2000) using the setup shown in figure 4(b). The telescope system was placed at ~2.5 m from the target center at angles between 0° and 22° with respect to the primary beam direction.

### 1.4. Electronics setup and analysis method

The data were recorded event-by-event using a VME (VERSA-Module Euro) based data acquisition system (Piersanti *et al* 2013) and analyzed with the scientific software framework ROOT (Brun and Rademakers 1997).

**1.4.1. Primary beam attenuation and fragments build-up.** For the attenuation measurements (figure 4(a)), the data acquisition system (DAQ) was triggered by the SC1 detector. Its analog signal, together with that from the ΔE and the E scintillators, were sent to different charge to digital converter (QDC) (CAEN V792N), where they were integrated over the selected gates. A scaler (CAEN V560) recorded the number of particles detected by SC1 (free trigger events) as well as the number of events acquired by the DAQ (accepted trigger events) and a pulse clock. The free and accepted trigger events were used to estimate the DAQ dead time as

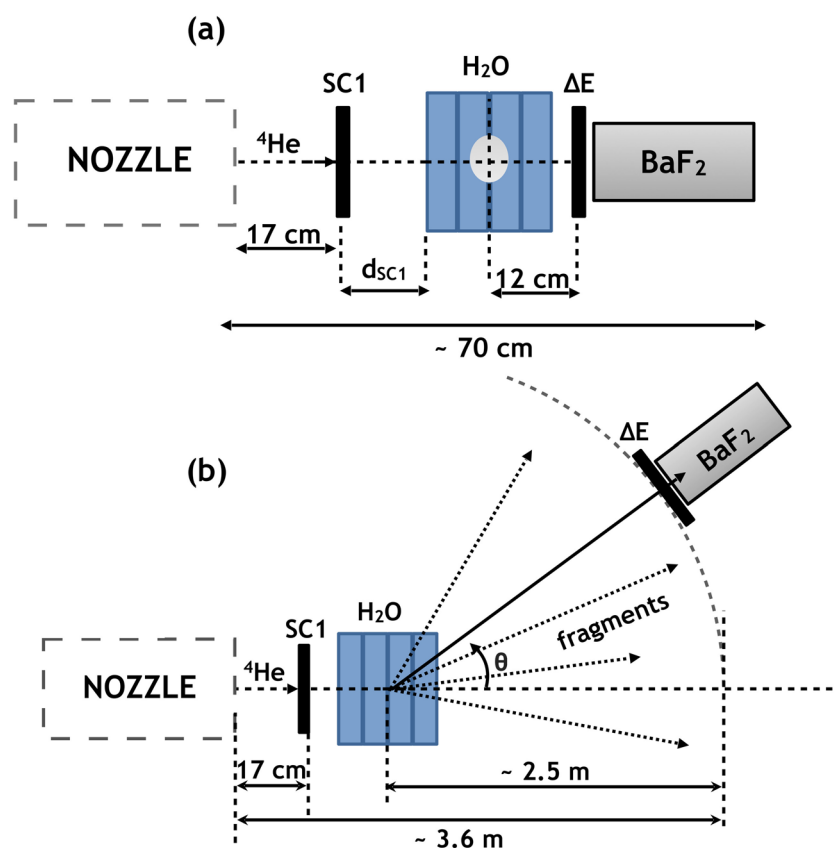


**Figure 4.** The experimental setup used to study the attenuation of the primary  $^4\text{He}$  beam flux is shown in (a). Kinetic energy and angular distribution have been measured with setup shown in (b). The figures are not in scale.

$$\text{dead time} = 1 - \frac{\text{acc trig}}{\text{free trig}} \quad (1)$$

The event rate was always set around  $1000 \text{ particle s}^{-1}$  to keep the dead time below 20%.

In the off-line analysis, the number of beam particles incident on the target was obtained from the pulse height spectrum of SC1 by selecting events within three standard deviations of the  $^4\text{He}$  peak. The total yield was defined as the ratio between the counts of a given ion type emerging from the target and the amount of primary particles impinging on the target. Particle identification in charge ( $Z$ ) and mass ( $A$ ) was accomplished by graphically selecting each fragment species in the two-dimensional (2D)-plot  $\Delta E$ - $E$  as shown in figure 5.

Together with single particle events, also multiplicity states like proton plus proton ( $p + p$ ), proton plus deuteron ( $p + d$ ) and proton plus triton ( $p + t$ ) can be also identified in figure 5. At an early stage of the analysis (Krämer *et al* 2016), the nature of those events could not be clearly assessed and thus they were only accounted for in the uncertainty estimate. However, in the final analysis presented in this work, they were selected graphically and classified as:

- events belonging to the  $p + p$  area are counted as two single protons;
- events belonging to the  $p + d$  area are counted as one proton and one deuteron;
- events belonging to the  $p + t$  area are counted as one proton and one triton.

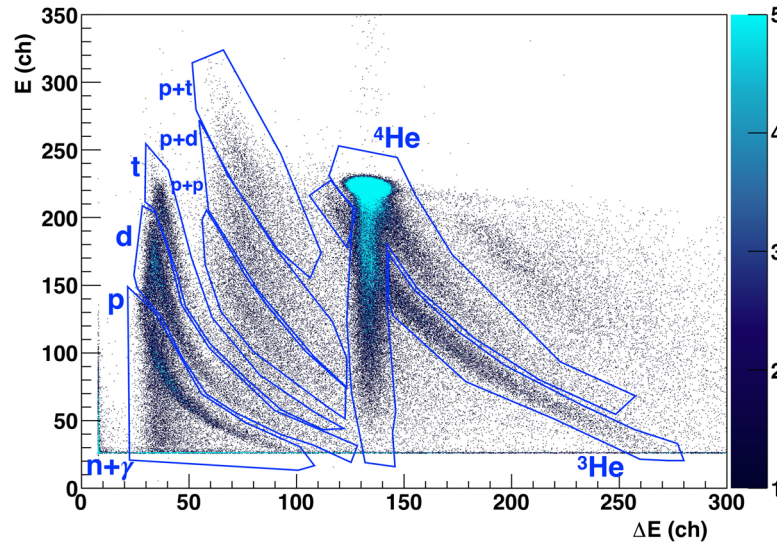


**Figure 5.**  $\Delta E$ - $E$  spectrum of  $200 \text{ MeV u}^{-1} {}^4\text{He}$  impinging on  $17 \text{ cm H}_2\text{O}$  target. The labels indicate all the different particle species including the non-charged ones. The contours are drawn as examples of handmade selection of each particle species.

The total yield of the H isotopes was then calculated as the sum of the contributions from multiple and single events.

**1.4.2. Angular distribution and kinetic energy spectra of  ${}^4\text{He}$  and secondary fragments.** To acquire only relevant events, the DAQ trigger was created by the coincidence between a signal from a primary ion, detected by SC1, and a surviving primary ion or fragment reaching the  $E$  detector. For each event, the TOF was recorded with a time to digital converter (TDC) (CAEN V775N), where the start signal was given by the trigger and the stop signal provided by the  $E$  scintillator. Furthermore, pulse height spectra of each detector were recorded with an analog to digital converter (ADC) after being amplified (AMP—CANBERRA 2022). To assess the number of  ${}^4\text{He}$  ions incident on the target, the discriminated SC1 signal was acquired with a scaler; triggering events, processed events and a pulse clock were counted as well.

The yield at a chosen angle (also referred to as partial yield) was calculated as the number of a given ion type detected at that location normalized by the number of primary particles incident on the target and by the solid angle covered by the detector. The total yield is then obtained by integrating the angular distribution in spherical variables.

The off-line analysis method exploited 2D scatter plots to identify particles in  $Z$  and  $A$ . Ions of different  $Z$  were graphically separated in the  $\Delta E$ - $E$  plot (as already shown in figure 5) and the selection applied to the  $E$ -TOF plot to discriminate the different isotopes (figures 6(b) and (c)).

Kinetic energy spectra of all fragment types were calculated using the TOF spectra (Gunzert-Marx *et al* 2008). The latter was first converted from TDC channels to nanosecond using no-target runs at  $0^\circ$  as calibration points. For a given particle, the calibrated TOF values were then converted into kinetic energy as

$$E_{\text{kin}} = \left[ \left( 1 - \left( \frac{d}{tc} \right)^2 \right)^{-1/2} - 1 \right] m_0 c^2 \quad (2)$$

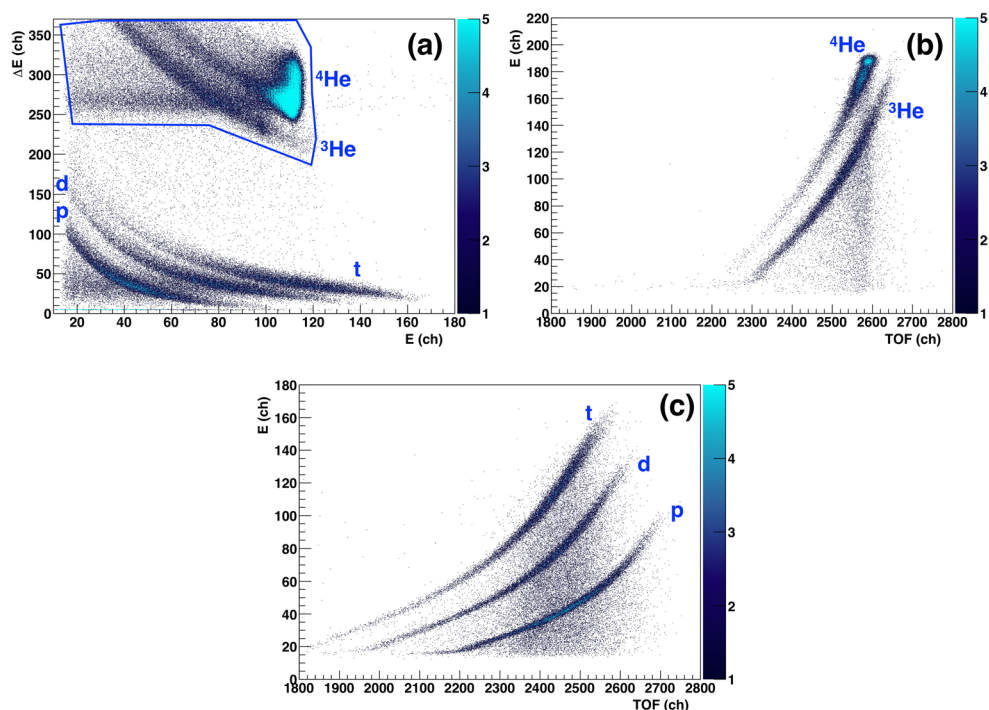


**Figure 6.** Examples illustrating the 2D-plot for  $120 \text{ MeV u}^{-1} {}^4\text{He}$  at 4 degree impinging 4.28 cm of water. In (a) graphical selection of events in the  $\Delta E$ - $E$  spectrum belonging to He. (b) Correlation between the  $E$  signal and the TOF signal after applying only the graphical selection illustrating in (b). (c) Resolution of H isotopes with  $E$  versus TOF after applying a graphical selection for H.

where  $m_0c^2$  is the particle rest mass,  $d$  the distance from the target center to the  $E$  detector and  $t$  the particle time-of-flight, i.e. the time needed by the fragment to travel from the target center to the  $E$  detector.  $t$  was determined as  $t_1 - t_2$ , where the former was the TOF value extracted from the calibrated TDC spectrum and the latter the time needed by a  ${}^4\text{He}$  ion to cover the distance between SC1 and the target center.  $t_2$  was calculated taking into account the theoretical flight time from SC1 to the mid-target and the energy loss along this path (by using LISE++ (Tarasov 2008)).

**1.4.3. Error estimation.** The error on the partial and total particle yields has a statistical and a systematic contribution. The number of recorded events for each measurement run is a compromise between three factors: beam time availability; minimization of the background coming from detector noise and fragmentation processes in the setup (beam line and detectors); acquisition of enough events to accurately characterize even the reaction channels with the lowest cross section.

However, the total uncertainty is dominated by the systematic error, which stems from the misidentification of particles in the 2D plots. To evaluate its weight, different selection methods have been considered to include or exclude events of ambiguous nature (Haettner *et al* 2013).

For the attenuation data, the alternative analysis procedure exploited only the energy spectrum of the  $\Delta E$  detector to obtain the yield of surviving fragments. In this case, the number of H and He ions could be obtained by fitting their corresponding peaks in the 1D energy spectrum with a

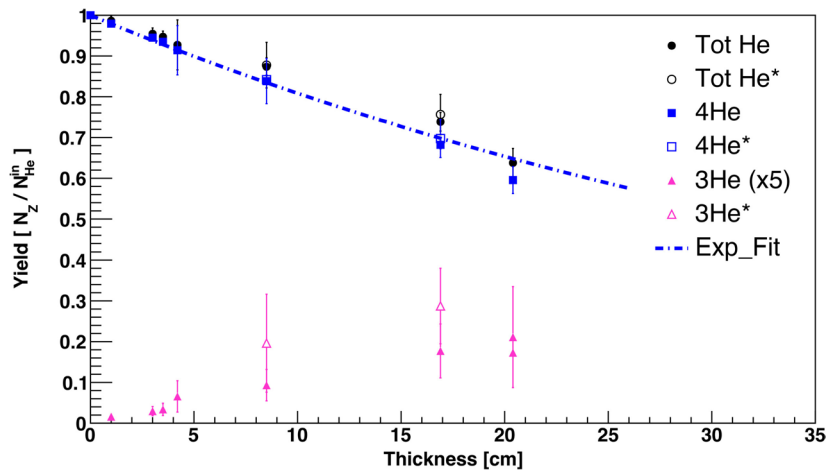


**Figure 7.** Attenuation curve of  $200 \text{ MeV u}^{-1} {}^4\text{He}$  and build-up of  ${}^3\text{He}$  as a function of depth in water. The data with open symbols, indicated with \* in the legend, were measured in another experiment with similar experimental setup. The  ${}^3\text{He}$  values were multiplied by a factor of 5 in order to have them more visible in a linear scale. The dashed line represents the exponential fit of the  ${}^4\text{He}$ , where the point measured at approximately 20 cm water depth was excluded from the fitting procedure because the residual energy of the beam dropped below the value for which the total fragmentation cross section is considered energy-independent. The attenuation of the total He (sum of  ${}^4\text{He}$  and  ${}^3\text{He}$ ) is also shown for comparison.

superposition of a Gaussian and a Landau function and integrating them. The comparison of the results between the one obtained with the 1D fit method and the 2D graphical approach provided an estimate of the efficiency for the latter, especially for counting low-energy fragments which could not reach the  $E$  detector. Furthermore, the importance of the overlapping regions between different particles types (represented by the Landau tail in the  $\Delta E$  spectrum) could be investigated with this test. These contributions were assessed and included in the systematic error.

The main source of uncertainty in the TOF measurements arises from the calibration method. Runs without target were acquired with three different beam energies to generate a calibration curve between TDC channels and time. The temporal resolution  $\Delta t$  was calculated from the FWHM of the primary beam TOF distribution without the target and it was found to be 0.66 ns at  $120 \text{ MeV u}^{-1}$  and 0.74 ns at  $200 \text{ MeV u}^{-1}$ .

The error propagation rules applied to equation (2) give the following formula for the uncertainty on the kinetic energy:

$$\frac{\Delta E}{E} = -\gamma(\gamma + 1) \frac{\Delta t}{t} \quad (3)$$

where  $\gamma$  is the relativistic Lorentz term, defined as  $\sqrt{1 - (\frac{v}{c})^2}$ .

However, due to the fact the TOF measurements have been performed with a thick target, the assumption that all the reactions happen at the center of the target was made. In order to quantify the error due to this approximation, the TOF was calculated considering two cases: when the reaction happens right at the beginning of the target and when the reaction happens at the end of the target. It was found a maximum difference in the TOF values of 9%.

**Table 1.** Mean free path  $\lambda$  and total fragmentation cross section  $\sigma_{\text{tf}}$  of 200 MeV  $\text{u}^{-1}$   $^4\text{He}$  in water. The error on the  $\lambda$  value was calculated by visually fitting lines with minimum and maximum slope. This approach is more conservative and results in a larger error with respect to the fit parameter error given by the standard mathematical program (12% against 5%). The total fragmentation cross section calculated with three different theoretical models (Kox *et al* 1987, Sihver and Mancusi 2009, Tripathi *et al* 1999) is reported for comparison.

	$\lambda$ (cm)	$\sigma_{\text{tf}}$ (mb)
This work	$47 \pm 6$	$636 \pm 17$
Kox <i>et al</i> (1987)	39	767
Sihver and Mancusi (2009)	37	798
Tripathi <i>et al</i> (1999)	42	706

## 2. Results

### 2.1. Primary beam attenuation and fragments build-up

The absorption of a 200 MeV  $\text{u}^{-1}$   $^4\text{He}$  beam as a function of depth in water and PMMA was measured by comparing the amount of ions impinging on the target to the number of those surviving after the target, as described in section 1.4.1. The results are shown in figure 7. While the  $^4\text{He}$  survival fraction decreases with increasing water depth due to nuclear fragmentation, the amount of  $^3\text{He}$  ions increases reaching its maximum before the Bragg peak. At this position, approximately  $0.69 \pm 0.03$   $^4\text{He}$  survive and  $0.05 \pm 0.02$   $^3\text{He}$  are produced.

As the  $^3\text{He}$  fragments build-up affects the behavior of the  $^4\text{He}$  curve, a separation of the two isotopes is necessary to obtain an accurate description of the  $^4\text{He}$  trend. The  $^3\text{He}$  nucleus is a neutron-deficient isotope and thus only one neutron can be lost in a nuclear interaction, which is named a ‘non charge-changing reactions’ (Schall *et al* 1996).

The trend of the  $^4\text{He}$  curve can be reproduced by the exponential function  $N_Z(x) = N_Z(0)e^{-x/\lambda_Z}$ , with  $N_Z$  the number of beam particles not undergoing fragmentation in the target of thickness  $x$  and  $\lambda$  the mean free path. Fitting the attenuation curve with this function provides an estimate of  $\lambda$  and of the ‘effective’ total fragmentation cross section  $\sigma_{\text{tf}} = \frac{1}{N_M\lambda}$  where  $N_M$  is the number of atoms or molecules per unit volume of the given absorber material. The values of  $\lambda$  and  $\sigma_{\text{tf}}$  measured in this work for the 200 MeV  $\text{u}^{-1}$  beam are reported in table 1 together with predictions from three theoretical models (Kox *et al* 1987, Tripathi *et al* 1999, Sihver and Mancusi 2009).

The primary beam attenuation was also investigated using PMMA targets and its results is plotted in figure 8 together with the curve measured in water and their corresponding fit functions. The difference between the two datasets increases with increasing target thickness, with survival in PMMA being always lower than water. This is translated in a higher  $\lambda$  for PMMA equal to  $45 \pm 4$  ( $\text{g cm}^{-2}$ ) ( $38.1 \pm 3.6$  cm) with a corresponding  $\sigma_{\text{tf}}$  of  $3698 \pm 340$  (mb).

The build-up of secondary fragments in water is shown in figure 9. The multiplicity issue described in section 1.4.1 affects mainly the protons yield, as indicated by the comparison between data with and without multiplicity contribution (empty and full symbols, respectively). At the Bragg peak position (25.6 cm  $\text{H}_2\text{O}$ ), 15% of total H is produced.

### 2.2. Angular distribution of $^4\text{He}$ and secondary fragments

Angular distributions of all particles were measured at  $0^\circ$ ,  $2^\circ$ ,  $4^\circ$ ,  $6^\circ$ ,  $8^\circ$ ,  $12^\circ$  and  $23^\circ$  ( $\pm 0.1^\circ$ ) with respect to the primary beam direction for 120 and 200 MeV  $\text{u}^{-1}$   $^4\text{He}$  ions interacting with

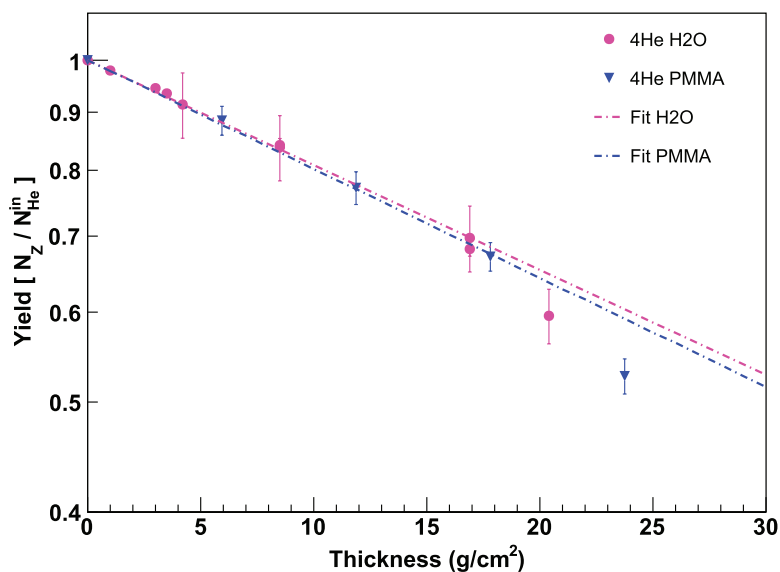


**Figure 8.** Fit function of the attenuation curves  $200 \text{ MeV u}^{-1} \text{ } ^4\text{He}$  as a function of depth impinging on water and PMMA targets.

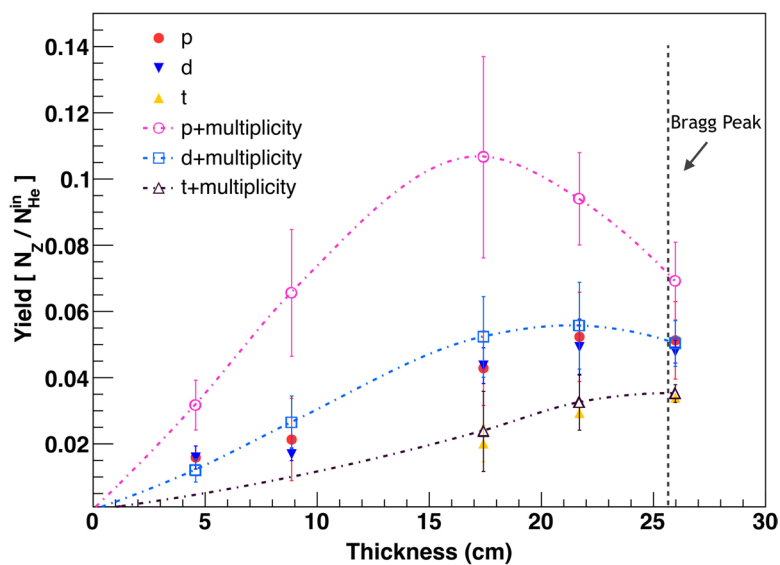


**Figure 9.** Build-up curves of protons, deuterons and tritons produced by  $^4\text{He}$  beam at  $200 \text{ MeV u}^{-1}$  impinging on water targets. The open symbols represent the point where the multiplicity states  $p + p$ ,  $p + d$  and  $p + t$  were accounted. The dashed line is only to guide the eye. The filled symbols represent the point without the multiplicity calculation, already published in Krämer *et al* (2016).

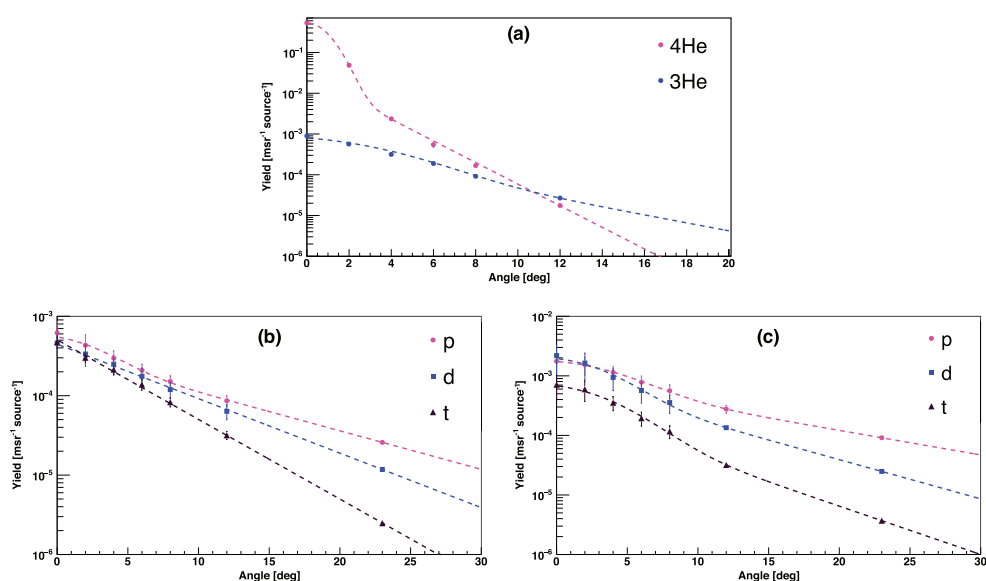


**Figure 10.** Angular distributions of primary  $^4\text{He}$  ions and secondary fragments measured at forward angles from  $0^\circ$  to  $20^\circ$ . The dashed lines represent the fit curves using a superposition of a Gaussian and an exponential function. The figure 10(a) presents the angular distribution of  $120 \text{ MeV u}^{-1} ^4\text{He}$  and the  $^3\text{He}$  produced. Figure 10(b) presents the angular distributions of the fragments produced by  $120 \text{ MeV u}^{-1} ^4\text{He}$  on  $4.28 \text{ cm H}_2\text{O}$  and the figure 10(c) represents the ones of the fragments produced by  $200 \text{ MeV u}^{-1} ^4\text{He}$  on  $13.96 \text{ cm H}_2\text{O}$ .

**Table 2.** Angular width of the radial distribution together with the integrated yield in two different angular ranges are reported. The integral of the radial distribution was calculated between  $0^\circ$  and  $23^\circ$ .

E	$120 \text{ MeV u}^{-1}$					$200 \text{ MeV u}^{-1}$				
	$^4\text{He}$	$^3\text{He}$	p	d	t	$^4\text{He}$	$^3\text{He}$	p	d	t
Yield $_{0^{23^\circ}}$	0.82	0.024	0.042	0.030	0.017	0.66	0.049	0.14	0.085	0.025
Yield $_{0^{90^\circ}}$	0.82	0.024	0.054	0.034	0.018	0.66	0.049	0.20	0.093	0.026
FWHM	$0.89^\circ$	$3.53^\circ$	$3.14^\circ$	—	—	$0.97^\circ$	$4.43^\circ$	$4.28^\circ$	$3.50^\circ$	$3.84^\circ$

$4.28 \text{ cm H}_2\text{O}$  and  $13.96 \text{ cm H}_2\text{O}$  targets, respectively. The angular distributions of all produced fragment species is the result of nuclear and scattering reactions and can be well described by a superposition of a Gaussian function (small angles below  $10^\circ$ ) and an exponential function for the tails at larger angles. Experimental results and fitting curves are plotted in figure 10(a) ( $^4\text{He}$  and  $^3\text{He}$ ) and figure 10(b) (H isotopes) for the  $120 \text{ MeV u}^{-1}$  beam and figure 10(c) (H isotopes) for the  $200 \text{ MeV u}^{-1}$  beam.

Total yields of each particle species are calculated by integrating the fitted curves in spherical variables. The results are reported in table 2. As the fitting functions can be extended to angles above  $23^\circ$ , an estimate of the total yield up to  $90^\circ$  could be obtained. The latter increases by 30% of the total yield for protons and 10% for deuterons. Yield values as well as FWHM of angular distributions for all particle types are presented in table 2.

The angular distributions of all fragments ( $^3\text{He}$ , p, d, t) are always much broader than that of the primary beam. For these energy-target thickness combinations, the angular distribution

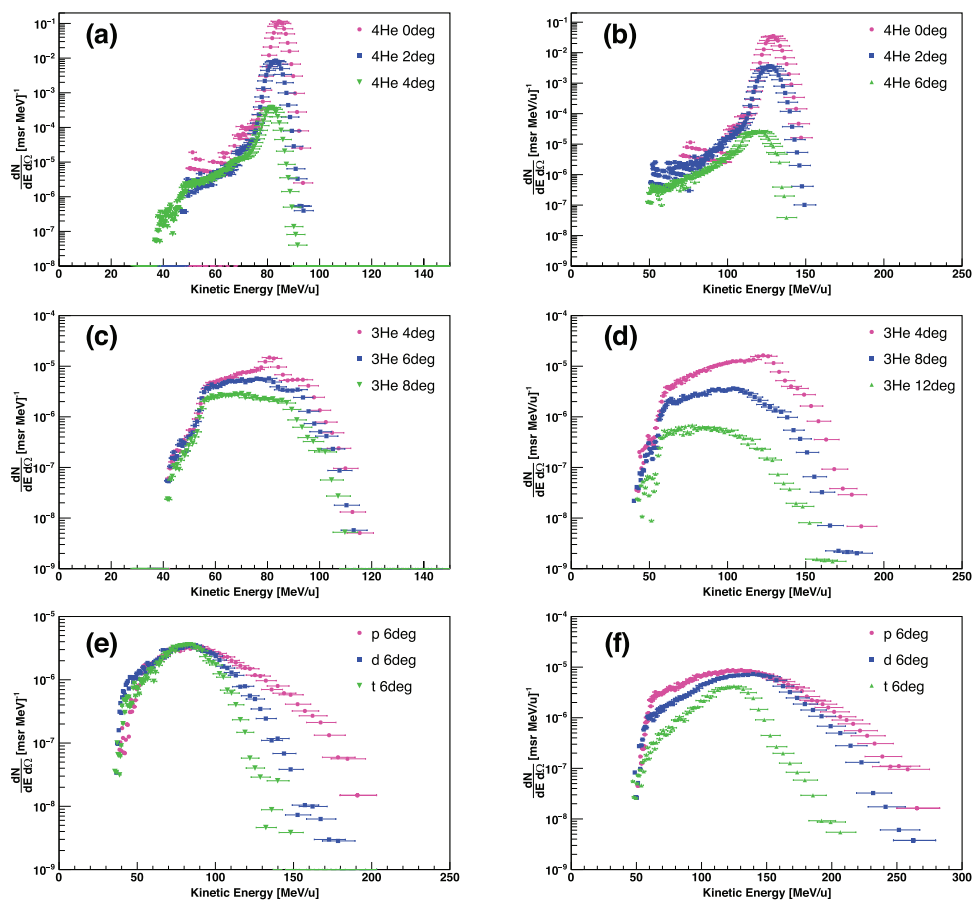


**Figure 11.** Kinetic energy spectra of secondary fragments produced by the interaction of  ${}^4\text{He}$  in water. Figures 11(a) and (b) show the kinetic energy spectra of the primary  ${}^4\text{He}$  ions with initial energy of  $120\text{ MeV u}^{-1}$  and  $200\text{ MeV u}^{-1}$  respectively. Figures 11(c) and (d) show the kinetic energy spectra of  ${}^3\text{He}$  produced by  $120$  and  $200\text{ MeV u}^{-1}$   ${}^4\text{He}$  on  $4.28$  and  $13.96\text{ cm}$  of water respectively. Kinetic energy spectra of protons, deuterons and tritons produced by  $120\text{ MeV u}^{-1}$  and  $200\text{ MeV u}^{-1}$   ${}^4\text{He}$  are shown in figures 11(e) and (f) respectively.

of the primary beams are comparable due to the presence of two opposing effects of lower energy and a thinner target.

The fitting curves as well as the corresponding FWHM values indicates that contribution of the exponential tails at large angles is much higher for H isotopes than for He independently of the primary beam energy.

Traces of  ${}^4\text{He}$  ions could be detected up to  $12^\circ$ . These ions have been classified as secondary  ${}^4\text{He}$  particles coming from elastic and quasi-elastic nuclear scattering of the primary beam with the target (Cucinotta *et al* 1993). Nevertheless, the comparison between the  $\text{Yield}_0^{23^\circ}$  and  $\text{Yield}_0^{90^\circ}$  shows that those events have a negligible contribution at large angles.

### 2.3. Energy spectra

The kinetic energy spectra of the primary ions as well as secondary fragments are calculated from the TOF spectra using equation (2). Examples are shown in figures 11(a) and (b) for

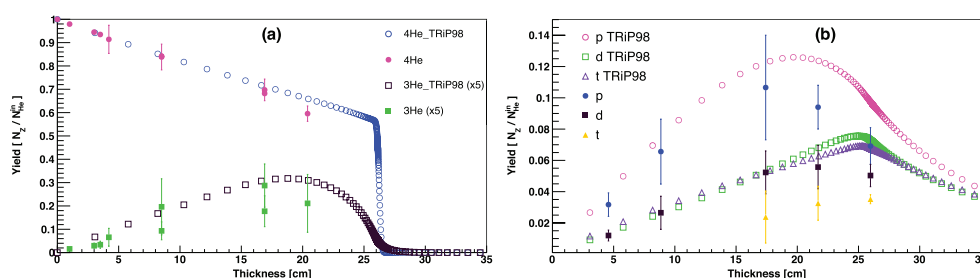


**Figure 12.** Comparison of  $^4\text{He}$  beam attenuation and build up of  $^3\text{He}$  (b) and protons, deuterons and tritons build-up (b) obtained from TRiP98. The data in (b) have been already presented in Krämer *et al* (2016). The open symbols represent the simulation and the filled ones the experimental data of this work.

primary ions at different angles. The spectrum at  $0^\circ$  peaks around  $130 \text{ MeV u}^{-1} \pm 10\%$  (initial energy  $200 \text{ MeV u}^{-1}$ ) and around  $84 \text{ MeV u}^{-1} \pm 7\%$  (initial energy  $120 \text{ MeV u}^{-1}$ ). The mean values were compared with predictions from LISE++ and found to be in agreement within 1% and 4%, respectively.

The kinetic energy spectra of secondary fragments produced by  $120$  and  $200 \text{ MeV u}^{-1}$   $^4\text{He}$  ions are shown in figures 11(c) and (d) ( $^3\text{He}$ ) and figures 11(e)–(f) (p, d, t). Below  $4^\circ$ ,  $^3\text{He}$  ions are characterized by a peak distribution centered at the residual primary beam energy while all H isotopes have much broader spectra with a tail extending above the initial value of the  $^4\text{He}$  projectiles. In particular, protons have a distinct broad distribution reaching energies higher than the primary beam energy. This phenomenon has been already observed (Gunzert-Marx *et al* 2008, Haettner *et al* 2013) and is associated to the Fermi momentum transferred by the nucleus to the fragment (Bertini *et al* 1976).

All distributions shift to lower energies and become broader at increasing angle.

### 3. Transport calculation with TRiP98

Transport calculations with the treatment planning system (TPS) TRiP98 (Krämer *et al* 2000) have been performed to reproduce the experimental data and their results are shown in figure 12. The latest version of TRiP98 (Krämer *et al* 2016) contains a new beam model for therapeutic  $^4\text{He}$  ions where the algorithms for describing the total reaction cross sections are from Tripathi's (Tripathi *et al* 1999) and Sihver's (Sihver and Mancusi 2009) models. The calculation of the primary beam attenuation is based on the nuclear collisions of  $^4\text{He}$  ions with protons and Oxygen to mimic a water target. Details can be found in Krämer *et al* (2016), where a comparison between TRiP98 predictions and a part of these experimental data was already presented.

Figure 12(a) shows a good agreement of the measured primary beam flux attenuation with the calculations, especially for thin targets. This result is a strong indication that even though no experimental data on total reaction cross sections are available between  $100$  and  $400 \text{ MeV u}^{-1}$  (Krämer *et al* 2016), the assumption of two-body dissociation of light ions to predict fragmentation cross sections is accurate. The model for predicting the production of  $^3\text{He}$  is also in good agreement with the experimental points.

A more accurate comparison between measured and predicted H isotopes yields than that reported in Krämer *et al* (2016) is shown in figure 12(b). The implementation of the multiplicity states (discussed in section 1.4.1) improved significantly the accuracy of proton and the deuteron yields, which appeared to be underestimated by  $\sim 50\%$  in the previous analysis

(Krämer *et al* 2016). However, protons are still underestimated by a factor of  $\sim 30\%$  because of emission at angles up to  $90^\circ$  (as shown in table 2).

#### 4. Discussion

The interaction of 120 and 200 MeV  $u^{-1}$   $^4\text{He}$  beams with water and PMMA targets has been investigated in this work. The experiments focussed on characterizing the primary beam attenuation and fragment build-up as a function of the target thickness as well as particle yields and kinetic energy spectra at several forward angles. The beam energies were selected because they are in the typical therapeutic range for cancer treatment and no experimental data were available (Krämer *et al* 2016). The choice of water as target material is most useful for clinical application and can be directly used as a benchmark of the physical model employed in TRiP98, and also as benchmark for Monte Carlo codes like Fluka (Böhlen *et al* 2014) and Geant4 (Agostinelli *et al* 2003). Thicknesses of 4.28 and 13.92 cm  $\text{H}_2\text{O}$  corresponding to approximately half of the  $^4\text{He}$  range at 120 (Bragg Peak at 10.5 cm  $\text{H}_2\text{O}$ ) and 200 (Bragg Peak at 25.8 cm  $\text{H}_2\text{O}$ ) MeV  $u^{-1}$ , respectively, were used.

The attenuation curve of the primary beam flux (figure 7) shows that the exponential behavior typical of  $^{12}\text{C}$  beams (Haettner *et al* 2013) cannot describe the He trend. After subtracting the contribution of  $^3\text{He}$  fragments (figure 7), the remaining curve can be described by a single exponential function and thus the mean free path  $\lambda$  and the 'effective' total fragmentation cross section  $\sigma_{\text{fr}}$  could be estimated. However, experiments with thick absorber are not optimal for an exact description of nuclear reaction cross sections and for this reason the notation 'effective' total fragmentation cross section have been used (Schall *et al* 1996). The results cannot not be compared with data from literature because no other measurements are available. Auce *et al* (1994), Ingemarsson *et al* (2000), Webber *et al* (1990), Ferrando *et al* (1988) and Jaros *et al* (1978), present charge- changing and total reaction cross section measurements in the low energy range (between 20 and 50 MeV  $u^{-1}$ ) and high energy range (above 500 MeV  $u^{-1}$ ).

Comparing the total reaction cross section of protons ( $\sigma_{\text{fr}} = 352$  mb (Schardt *et al* 2010)),  $^4\text{He}$  ( $\sigma_{\text{fr}} = 636$  mb) and  $^{12}\text{C}$  ( $\sigma_{\text{fr}} = 1424$  mb (Schardt *et al* 2010)) at a given water target thickness, it is possible to observe how the value rises with increasing projectile charge due to the contribution of different reaction mechanisms (deep inelastic collisions or fusion reactions) (Schardt *et al* 2010). The possible reaction channels for light fragments production in  $^4\text{He}$  collisions with hydrogen and oxygen are only six in total (Krämer *et al* 2016) and thus lead to a higher survival fraction than carbon ions (Burigo *et al* 2014). At 8 cm water depth, the survival fraction of  $^4\text{He}$  ions is 16% higher than  $^{12}\text{C}$  ions (Haettner *et al* 2013) while at 20 cm depth, i.e. slightly before the Bragg peak,  $65 \pm 5\%$  of primary  $^4\text{He}$  do not undergo fragmentation (figure 7) versus 38% of primary  $^{12}\text{C}$  ions.

The angular distributions of all secondary fragments ( $^3\text{He}$ , p, d, t) are much broader than the primary beam, extending well above  $20^\circ$ . This gives information on the fragmentation processes as well as nuclear and Coulomb multiple scattering. Therefore, the implementation of the lateral beam profile, including secondary particles, in the treatment planning systems is fundamental in order to better describe the core and the halo of the beam (Gottschalk *et al* 2015). Furthermore, all H isotopes have broad energy distribution, with a tails extending up to twice the energy of the primary beam. However, the dose contribution at these energies is much smaller when compared to the primary beam energy as the small size of the tail in the Bragg curve indicates.

$^4\text{He}$  ions can be detected up to  $12^\circ$  (figure 10(a)) while carbon ions do not scatter above  $5^\circ$ . For a given particle with charge  $Z$  and the mass  $M$ , the multiple scattering depends on the ratio between  $Z$  and  $M$  and thus, at the same velocity,  $^4\text{He}$  projectiles suffer more lateral scattering

than a Carbon beam. Additionally, the cross section for nuclear elastic scattering is higher for  $^4\text{He}$  ions than for  $^{12}\text{C}$ . As both types of scattering processes affect more  $^4\text{He}$  than  $^{12}\text{C}$  ions, the former will be found at larger angles than the latter.

## 5. Conclusion

In summary,  $^4\text{He}$  particles have less attenuation and smaller tail in the dose profile than  $^{12}\text{C}$  ions, suffer less scattering than protons and have a moderate linear energy transfer (LET) closer to  $^{12}\text{C}$  ions than to protons. The results obtained by the current studied support the statement already made by the studies of Grün *et al* (2015) and Knäusl *et al* (2016) that even though an optimal particle species for all cancer types might not exist,  $^4\text{He}$  ions seem very promising especially for the treatment of pediatric patients.

Future investigations will focus on systematic studies at different target thicknesses and beam energies between 50 and 250 MeV  $\text{u}^{-1}$  in order to cover the literature ‘gap’ and extend the TRiP98 database. Moreover, it will be important to characterize the production of secondary neutrons.

## Acknowledgments

We wish to thank Dr Thomas Haberer for providing the beam time necessary to complete this investigation and the accelerator staff for their excellent support. Thanks to Dr Sebastian Hild for proofreading the manuscript. This work is part of the HGS-HiRE program.

## References

- Agostinelli S *et al* 2003 Geant4—a simulation toolkit *Nucl. Instrum. Methods Phys. Res. A* **506** 250–303
- Auce A, Carlson R F, Cox A J, Ingemarsson A, Johansson R, Renberg P U, Sundberg O, Tibell G and Zorro R 1994 Reaction cross sections for 75–190 MeV alpha particles on targets from  $^{12}\text{C}$  to  $^{208}\text{Pb}$  *Phys. Rev. C* **50** 871
- Bertini H W, Santoro R T and Hermann O W 1976 Calculated nucleon spectra at several angles from 192-, 500-, 700-, and 900-MeV  $^{12}\text{C}$  on  $^{56}\text{Fe}$  *Phys. Rev. C* **14** 590
- Böhlen T, Cerutti F, Chin M, Fassò A, Ferrari A, Ortega P, Mairani A, Sala P, Smirnov G and Vlachoudis V 2014 The FLUKA code: developments and challenges for high energy and medical applications *Nucl. Data Sheets* **120** 211–4
- Brun R and Rademakers F 1997 Root—an object oriented data analysis framework *Nucl. Instrum. Methods A* **389** 81–6
- Burigo L, Pshenichnov I, Mishustin I and Bleicher M 2014 Microdosimetry spectra and RBE of  $^1\text{H}$ ,  $^4\text{He}$ ,  $^7\text{Li}$  and  $^{12}\text{C}$  nuclei in water studied with Geant4 *Nucl. Instrum. Methods Phys. Res. B* **320** 3698–711
- Carboni S *et al* 2012 Particle identification using the (DELTA)E-E technique and pulse shape discrimination with the silicon detectors of the FAZIA project *Nucl. Instrum. Methods Phys. Res. A* **664** 251–63
- Cucinotta F L, Townsend W and Wilson J W 1993 Description of alpha-nucleus interaction cross sections for cosmic ray shielding studies *NASA Tech. Pap.* **3285** 1–42
- Durante M and Loeffler J S 2010 Charged particles in radiation oncology *Nat. Rev. Clin. Oncol.* **7** 37–43
- Durante M and Paganetti H 2016 Nuclear physics in particle therapy: a review *Rep. Prog. Phys.* **79** 096702
- Ferrando P, Webber W R, Goret P, Kish J C, Schrier D A, Soutoul A and Testard O 1988 Measurement of  $^{12}\text{C}$ ,  $^{16}\text{O}$ , and  $^{56}\text{Fe}$  charge changing cross sections in helium at high energy, comparison with cross sections in hydrogen, and application to cosmic-ray propagation *Phys. Rev. C* **37** 1490–501
- Fuchs H, Strobele J, Schreiner T, Hirtl A and Georg D 2012 A pencil beam algorithm for helium ion beam therapy *Med. Phys.* **39** 6726–37

- Gottschalk B, Cascio E W, Daartz J and Wagner M S 2015 On the nuclear halo of a proton pencil beam stopping in water *Phys. Med. Biol.* **60** 5627
- Grün R, Friedrich T, Krämer M, Zink K, Durante M, Engenhardt-Cabillic R and Scholz M 2015 Assessment of potential advantages of relevant ions for particle therapy: a model based study *Med. Phys.* **42** 1037–47
- Gunzert-Marx K, Iwase H, Schardt D and Simon R S 2008 Secondary beam fragments produced by 200 MeV/u  $^{12}\text{C}$  ions in water and their dose contributions in carbon ion radiotherapy *New J. Phys.* **10** 075003
- Haberer T, Debus J, Eickhoff H, Jäkel O, Schulz-Ertner D and Weber U 2004 The Heidelberg Ion Therapy Center *Radiother. Oncol.* **73** S186–90
- Haettner E, Iwase H, Krämer M, Kraft G and Schardt D 2013 Experimental study of nuclear fragmentation of 200 and 400 MeV/u  $^{12}\text{C}$  ions in water for applications in particle therapy *Phys. Med. Biol.* **58** 8265–79
- Ingemarsson A et al 2000 New results for reaction cross sections of intermediate energy  $\alpha$  particles on targets from  $^9\text{Be}$  to  $^{208}\text{Pb}$  *Nucl. Phys. A* **676** 3–31
- Jaros J et al 1978 Nucleus–nucleus total cross sections for light nuclei at 1.55 and 2.89 GeV/c per nucleon *Phys. Rev. C* **18** 2273–92
- Knäusel B, Fuchs H, Dieckmann K and Georg D 2016 Can particle beam therapy be improved using helium ions?—A planning study focusing on pediatric patients *Acta Oncol.* **55** 751–9
- Kox S et al 1987 Trends of total reaction cross sections for heavy ion collisions in the intermediate energy range *Phys. Rev. C* **35** 1678–91
- Krämer M et al 2016 Helium ions for radiotherapy? Physical and biological verification of a novel treatment modality *Med. Phys.* **43** 1995
- Krämer M, Jäkel O, Haberer T, Kraft G, Schardt D and Weber U 2000 Treatment planning for heavy-ion radiotherapy: physical beam model and dose optimization *Phys. Med. Biol.* **45** 3299–317
- Loeffler J S and Durante M 2013 Charged particle therapy—optimization, challenges and future directions *Clin. Oncol.* **10** 411–24
- Mairani A et al 2016 Biologically optimized helium ion plans: calculation approach and its *in vitro* validation *Phys. Med. Biol.* **61** 4283–99
- Marafini M et al 2017 Secondary radiation measurements for particle therapy applications: nuclear fragmentation produced by  $^4\text{He}$  ion beam in a PMMA target *Phys. Med. Biol.* accepted
- Piersanti L, Schuy C, La Tessa C and Durante M 2013 Development of a VME data acquisition system *Technical Report GSI* (<http://repository.gsi.de/record/52370>)
- PTW 2015 Measurements of spread-out-bragg-peaks with the PEAKFINDER and MP3-P Technical Note D901.200.00/00 en PTW-Freiburg
- Schall I et al 1996 Charge-changing nuclear reactions of relativistic light-ion beams ( $5 \leq z \leq 10$ ) passing through thick absorbers *Nucl. Instrum. Methods Phys. Res. B* **117** 221–34
- Schardt D, Elsässer T and Schulz-Ertner D 2010 Heavy-ion tumor therapy: physical and radiobiological benefits *Rev. Mod. Phys.* **82** 383
- Sihver L and Mancusi D 2009 Present status and validation of HIBRAC *Radiat. Meas.* **44** 38–46
- Taleei R, Guan F, Peeler C, Bronk L, Patel D, Mirkovic D, Grosshans D R, Mohan R and Titt U 2016 Monte carlo simulations of  $^3\text{He}$  ion physical characteristics in a water phantom and evaluation of radiobiological effectiveness *Med. Phys.* **43** 761–76
- Tarasov O 2008 LISE++: radioactive beam production with inflight separators *Nucl. Instrum. Methods B* **266** 4657–64
- Tommasino F, Scifoni E and Durante M 2015 New ions for therapy *Int. J. Part. Ther.* **2** 428–38
- Tripathi R K, Cucinotta F A and Wilson J W 1999 Accurate universal parameterization of absorption cross sections III—light systems *Nucl. Instrum. Methods Phys. Res. B* **155** 349–56
- Webber W R, Kish J C and Schrier D A 1990 Total charge and mass changing cross sections of relativistic nuclei in hydrogen, helium, and carbon targets *Phys. Rev. C* **41** 520
- Weber U and Kraft G 2009 Comparison of carbon ions versus protons *Cancer J.* **15** 325–32
- Weimar R, Romberg R, Frigo S, Kasshke B and Feulner P 2000 Time-of-flight techniques for the investigation of kinetic energy distributions of ions and neutrals desorbed by core excitations *Surf. Sci.* **451** 124–9
- Zhu X R, Jursinic P A, Grimm D F, Lopez F, Rownd J J and Gillin M T 2002 Evaluation of Kodak EDR2 film for dose verification of intensity modulated radiation therapy delivered by a static multileaf collimator *Med. Phys.* **29** 1687–92